Design of Negative Curvature Hollow Core Fiber Based on Reinforcement Learning

Xiaowen Hu and Axel Schülzgen, *Fellow, OSA*

***Abstract*—In negative curvature hollow core fibers (NCHCFs), light guidance is based on the capillary structure in the cladding. To achieve desirable fiber propagation properties, various designs of the capillary structure have been proposed in literature. However, the design process so far depends more or less on experience. In this article, we propose a reinforcement learning (RL) based method of systematically optimizing the capillary structure to achieve low average confinement loss (CL) for a given operating wavelength range and core radius. We use a recurrent neural network (RNN) to interactively study the properties of different capillary structures. The wavelength averaged CLs of the resulting designs are more than one order of magnitude lower than the lowest average CL of prior designs in literature. The same approach can be applied to search for optimum capillary structures in terms of other fiber propagation properties such as bending loss (BL), higher order modes extinction ratio (HOMER), overlap of the optical mode with the capillary structure, or a trade-off among these properties.**

***Index Terms*—Negative curvature hollow core fiber, optical fiber design, reinforcement learning.**

I. Introduction

SINCE their first proposal [1], [2], negative curvature hollow core fibers (NCHCFs) have triggered a lot of interest due to their low losses over a wide wavelength span and freedom in design when compared to other hollow core fibers (HCFs) such as hollow core photonic bandgap fibers (HC-PBGFs) [3]. The light guidance in NCHCFs is achieved by inhibited coupling (IC) between the core modes and cladding modes. The low loss transmission windows are determined by the cladding capillary thickness according to the anti-resonant reflecting optical waveguide (ARROW) model [4]–[6]. The three main parameters that characterize the performance of a NCHCF are mode attenuation, bending loss (BL) and higher order modes extinction ratio (HOMER). There are three loss mechanisms that result in mode attenuation: confinement loss (CL), surface scattering loss (SSL) and material absorption. CL, which relates to the leaky nature of the guided modes, is the dominant loss mechanism in the near infrared region [7]. Reducing CLs is crucial for NCHCFs to be used in long-haul telecommunication systems in replacement of conventional silica solid core fibers. SSL [8], [9] is caused by the surface roughness introduced by frozen surface capillary waves (SCWs) during the fiber draw process. It is the factor that limits the bandwidth of HC-PBGFs [10]. Material absorption is negligible when NCHCFs are operating at telecommunication wavelengths, where fused silica has ultra-low losses. However, it becomes dominant in the far infrared and terahertz region [7]. It is known that reducing the overlap between the light field and the glass structure can result in lower SSL [3] and lower material absorption. BL refers to the attenuation of modes when the fiber is bent. It has been shown [11] that bending can lead to a high frequency edge shift of the high loss peaks and introduce additional loss peaks to the CL spectrum where phase-matching conditions are satisfied. Low BL is also of high importance in light delivery applications. HOMER, defined as the ratio of the lowest CL of higher order modes (HOMs) to the CL of the fundamental mode, characterizes the fiber's ability of single-mode operation. In NCHCFs, all HOMs exist at the same time without cut-off condition. Although HOMs are rarely observed in NCHCFs in long-haul transmission because of their high CLs [12], they degrade the output beam quality of shorter fibers. High HOMER is favorable in applications such as laser beam machining and pulse compression. Because of the IC guidance of modes in NCHCFs, CL, BL, HOMER and overlap of the optical mode with the capillary structure have a strong dependence on the cladding structures. Thus, much effort has been made to study the relationship between cladding structures and the properties of NCHCFs. There have been two main design strategies. On one hand, analytical models have been proposed to study the guiding mechanism of NCHCFs, such as the ARROW model [4]–[6], the coupled-mode model [13]–[15] and several others [11], [16]–[21]. Numerical methods have also been used to study the effects of geometrical parameters on the guiding properties [12], [22]–[26]. Nevertheless, the analytical models are based on simplified fiber structures from the actual NCHCFs whereas the numerical methods are either focused on specific geometrical features or on conventional NCHCFs with circular capillary tubes [1], [2]. Both approaches are far from providing comprehensive guidelines on NCHCF designs. On the other hand, besides the conventional circular-tube NCHCFs, novel designs of NCHCFs have been developed more or less empirically, including NCHCFs with nested tubes [7], [27], with elliptical tubes [28]–[31], with semi-circular nested tubes [32],

Manuscript received September 26, 2019; revised January 14, 2020; accepted February 2, 2020. Date of publication February 6, 2020; date of current version April 1, 2020. This work was supported in part by the United States Army Research Office under Grant W911NF-12-1-0450, Grant W911NF-17-1-0501, and Grant W911NF-19-1-0426, and in part by the United States Air Force Office of Scientific Research under Grant FA9550-15-10041. *(Corresponding author: Xiaowen Hu.)*

The authors are with the University of Central Florida, Orlando, FL 32816 USA (e-mail: steven.hu@knights.ucf.edu; axel@creol.ucf.edu).

This article has supplementary downloadable material available at https://ieeexplore.ieee.org, provided by the authors.

Color versions of one or more of the figures in this article are available online at https://ieeexplore.ieee.org.

Digital Object Identifier 10.1109/JLT.2020.2971943

with adjacent nested tubes [33], [34], with radially asymmetric nodeless claddings [35], with nested positive and negative curvatures [36], with nested tubes and supporting rods [37], with square cores [38], with lotus-shaped negative curvature [39] and with conjoined tubes [40]. Among these designs, NCHCFs with circular tubes, with nested tubes, with lotus-shaped negative curvature and with conjoined tubes have been fabricated, of which the lowest measured losses are 7.7 dB/km at 750 nm [15], 1.3 dB/km at 1450 nm [41], 10 dB/km at 1550 nm [39], and 2 dB/km at 1512 nm [40], respectively. However, despite a few guidelines such as applying negative curvatures [24] and avoiding touching points between cladding capillaries [22], the design process so far relies much on experience.

Today, the rapid development of machine learning opens another possibility of solving the NCHCF design problem. As a branch of machine learning, reinforcement learning (RL) is an algorithm that mimics the animals' trial-and-error learning [42]. Unlike supervised learning [43] where the best action possible is given by an instructor with a set of labeled examples, RL agents evaluate an action by interacting directly with their environment and improve their performance over time. The basic scenario of an RL system is an iterative process. The decision-making agent first perceives the information about the current environment, called state. The agent then takes an action according to the current state and its way of behaving, or its policy. Finally, after an action has been taken, the environment gives the agent a reward and transforms to a new state. The goal of the agent is to accumulate the most rewards by improving its policy over time. Recent years have witnessed many interactions between the field of optics and RL. RL has been successfully applied in optical systems such as optical communication networks [44] and photonic reservoir computing [45]. Optical methods have also been implemented in RL tasks, e.g. randomness generation using laser chaos signal [46] and stigmergic signal processing using solitonic waveguides [47].

In this paper, we treat the problem of NCHCF design as a multi-armed bandit (MAB) problem [48], [49] in the context of RL, where the best action is only to be learned in one state. Specifically, the structure in the cladding is expressed as a stack of small capillary segments. Different stacks of individual small segments form the state space of all possible structures. With the choices of reward signal related to CL, BL, HOMER, overlap of the optical mode with the capillary structure, or a combination of these parameters, the problem of finding the optimum design is converted to finding the combination of the small segments in the state space with favorable rewards. By applying the RL method, we demonstrate, for the first time to the best of our knowledge, a systematic way of designing the cladding structure in NCHCFs. As an example, we show the design process of finding the cladding structure with low average CL in a specific range of operating wavelengths for a selected core radius.

II. Method

As a proof of concept, NCHCFs with eight symmetrically arranged capillary structures in the cladding are studied. The area to be designed is indicated as section ① in Fig. 1(a), where a sample capillary structure is also shown. The structure is formed by adding small segments of circular rings one after another (Fig. 1(b)). Each segment has the same midline length l but a different radius r_i. Three quantities that uniquely define the i-th segment are: the position of the ending point P_i: (x_i, y_i), the angle between the horizontal line and the tangent line at P_i: β_i, and the angle between the tangent lines at P_{i-1} and $P_{i-1}P_i$: α_i. The iterative relation between the i-th segment and the (i−1)-th segment can be deduced from the geometrical relations:

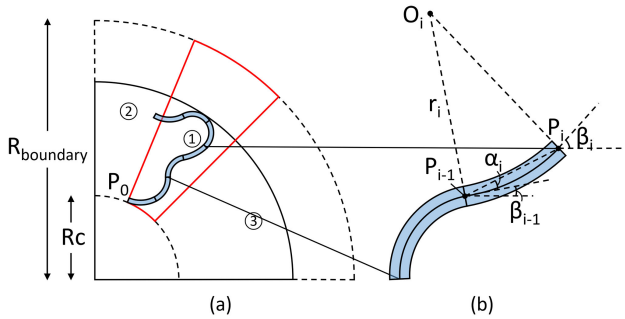

Fig. 1. (a) Schematic diagram of the quarter hollow core fiber cross section. R_c and $R_{boundary}$ are the core radius and the largest possible radius of the fiber, respectively. The area to be designed is section ① within the boundary indicated by the red lines. P_0 is the starting point of the design process. An arbitrary capillary structure (light blue) is shown as an example. The final radius of the fiber cladding is determined by the furthest distance from the capillary to the center. (b) Enlarged diagram of two segments in (a) showing the procedure of attaching additional segments.

$$r_i = \frac{90l}{\alpha_i \pi} \tag{1}$$

$$\beta_i = 2\alpha_i + \beta_{i-1} \tag{2}$$

$$x_i = x_{i-1} + 2r_i \sin\alpha_i \cos\left(\alpha_i + \beta_{i-1}\right) \tag{3}$$

$$y_i = y_{i-1} + 2r_i \sin\alpha_i \sin\left(\alpha_i + \beta_{i-1}\right) \tag{4}$$

In the case of a rectangular segment, $\beta_i = \beta_{i-1}$, and x_i, y_i are simply given by:

$$x_i = x_{i-1} + l\cos\beta_{i-1} \tag{5}$$

$$y_i = y_{i-1} + l\sin\beta_{i-1} \tag{6}$$

All angles in Equation (1)–(6) are in degrees. Angles measured in the anticlockwise direction are positive and vice versa. Thus, given the position of the starting point P_0: (x_0, y_0) and the starting angle β_0, the final capillary structure can be expressed by a sequence of angles: $(\alpha_1, \alpha_2, \cdots, \alpha_n)$. For the geometry shown in Fig. 1(a), $\beta_0 = -22.5°$.

In the structure generation phase, the angles α_i are randomly picked from $-55°$ to $55°$ with intervals of $5°$ for all segments except for the first one, of which the angle α_1 is between $15°$ and $55°$ in order to prevent trivial structures. The structure generation process terminates when any of the following three conditions is met: (i) the number of segments reaches the maximum number of 20, (ii) the ending point of the capillary exceeds the boundary indicated by the red lines in Fig. 1(a), or (iii) a termination signal is received. The resulting sequence of angles is then added to

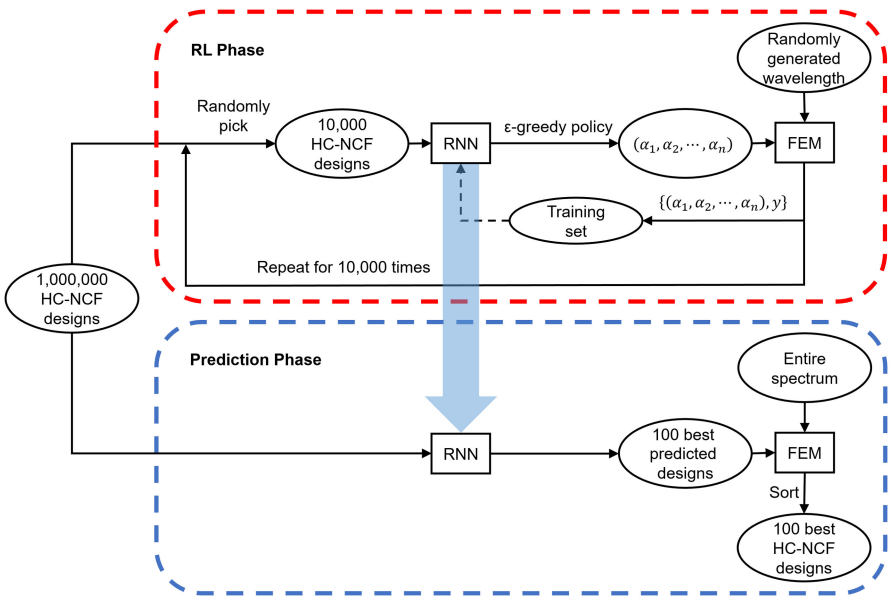

Fig. 2. Flowchart of the RL based NCHCF design process. The steps indicated by solid arrows are executed every time when encountered. The dashed arrow from the training set to the RNN means the whole training set is used to train the RNN every time when 100 new training pairs are added to the training set. After the RL phase finishes, the trained RNN is passed to the prediction phase (light blue arrow).

the set of designs if no identical sequence already exists. With this procedure, a set of 1,000,000 different NCHCF structures is generated.

In the structure evaluation phase, where the CL of each structure is calculated, angles are loaded from the sequence one by one until the midline of one segment reaches the boundary. The part of the segment outside of the boundary is truncated and the remaining angles in the sequence are discarded. The furthest distance from the center of the fiber to the capillary structure is then calculated, which determines the inner radius of the fiber outer cladding tube. The structure in section ① is flipped symmetrically to section ② to form the complete unit of the capillary structure. The unit structure is then repeated in section ③ to form the complete quarter cross-section of the hollow core fibers.

The capillary thickness of each segment is selected as 100 nm, a thickness for which the first transmission window is centered at 287 nm. For any intended operating wavelength, the required capillary thickness can be easily deduced from the ARROW model [4]–[6]. In our simulations, the midline length l of each segment is 2 μm and the core radius R_c is 4.9 μm. These geometrical parameters are chosen because for this given core radius, they enable a minimum loss design for a circular-tube NCHCF (Fig. 5 black squares) in the structure generation process (with α constantly equals to 20°). The maximum radius of the cross-section $R_{boundary}$ is 15 μm.

The RL based design process consists of two phases: the RL phase and the prediction phase (Fig. 2). In each step of the RL phase, a subset of 10,000 NCHCF designs are randomly picked from the previously-generated design set and fed into a recurrent neural network (RNN) [50]. The RNN then selects a design using an ε-greedy policy, that is, selecting the best predicted design with probability (1-ε) and selecting a design randomly with probability ε. ε remains 1 for the first 100 simulations, linearly decreases from 0.9 to 0.1 over the 101st to the 8,000th simulations and stays fixed at 0.1 over the remaining 2,000 simulations. Once a design is selected, its CL at a randomly chosen wavelength between 240 nm and 390 nm is calculated using a full vector finite-element method (FEM) based modal solver COMSOL Multiphysics with MATLAB. The mesh size and perfectly-matched layer (PML) parameters have been adjusted until a convergence test is passed. The refractive index of silica is set to be 1.45. To fully distinguish different CL levels and take advantage of the nonlinear rectified linear unit (ReLU) [51], the ground truth is expressed as $y = \log_{10} CL + 10$. The pair of sequence of angles and ground truth y is then added to a training set. The RNN is trained with the training set every time when 100 new training pairs are added to the training set. The whole process is repeated 10,000 times before the trained RNN is transferred to the prediction phase. In the prediction phase, the RNN selects the top 100 designs with the lowest predicted CLs among the total 1,000,000 different NCHCF designs. FEM calculations of the CL spectra of these 100 designs are performed every 10 nm between 240 nm and 390 nm. Finally, these 100 designs are sorted according to their average CLs over this wavelength range.

The architecture of the RNN is shown in Fig. 3. To improve efficiency in training, all the sequences of angles are masked to the same length of 20 with a mask value of 100. The sequence of angles is normalized and passed through two blocks. Each block has one Long Short Term Memory (LSTM) [52] layer with 128 hidden units, followed by a batch normalization layer and a ReLU layer. The LSTM layer in the first block returns the full sequence whereas the one in the second block only returns the last output. Before giving the prediction $\hat{y}$, the output after the two blocks is further passed through two dense layers with

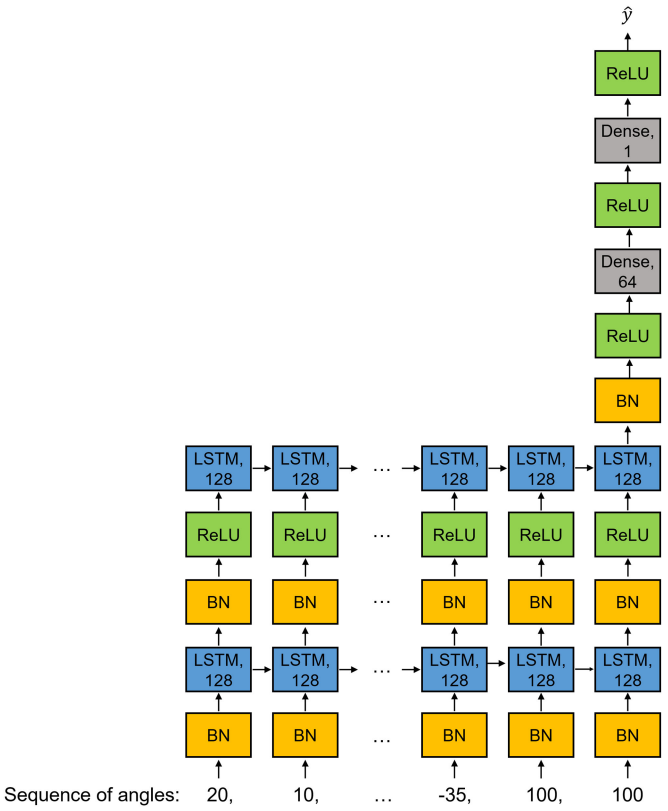

Fig. 3. Schematic of the RNN architecture. An arbitrary sequence of angles is shown as an example. Before fed into the RNN, the sequence of angles is masked to the maximum length of 20 with a mask value of 100.

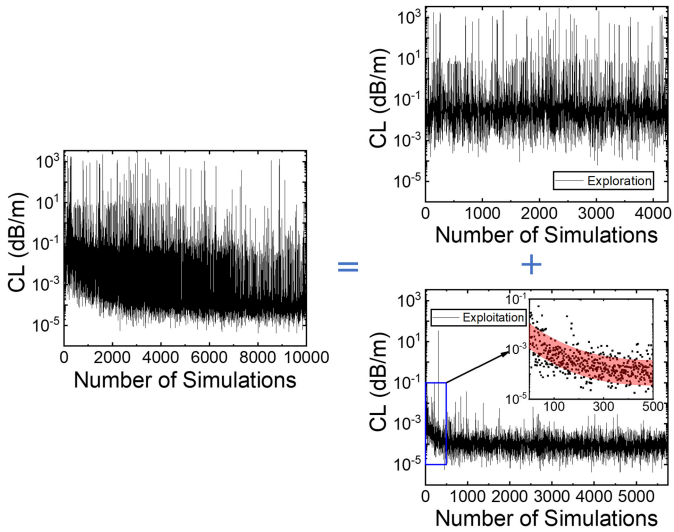

Fig. 4. Left: The learning curve during the NCHCF design process. It can be divided into exploration part (Top right) and exploitation part (bottom right). Inset: CLs of the first 500 simulations in the exploitation part indicating the order of magnitude improvement during exploitation (red area is guidance for the eyes).

ReLU as the activation function. The first dense layer has 64 output units and the second dense layer has 1 output unit. After the forward propagation, the mean absolute error between the prediction and ground truth is used as the loss function in the back propagation [53]. The weights in the RNN are initialized using the Xavier initializer [54] and updated using the adaptive moment estimation (Adam) [55] optimizer algorithm with a learning rate of 0.005, a gradient momentum of 0.9, a gradient root mean square propagation (RMSProp) of 0.99, and decay rate of 0.005. The RNN is trained for 10 epochs. In each epoch, the training set is shuffled and divided into minibatches. The size of the minibatches is 10 when the number of training pairs is below 3000 and 100 when larger than 3000.

III. Results

The NCHCF design process takes about 3.7 days on a personal computer with AMD Ryzen Threadripper 1950X 16-core processor, NVIDIA GeForce GTX 750 Ti graphics card and 128 GB memory. Fig. 4 (left) shows the CL as a function of the number of simulations, which represents the learning curve during the RL phase. It can be divided into two parts: exploration (Fig. 4 top right), where the RL agent constantly explores the state space by randomly selecting a structure, and exploitation (Fig. 4 bottom right), where the structure with the lowest predicted average CL among the subset is selected. The effectiveness of the RL phase can be seen from the order of magnitude improvement and subsequent convergence of the CLs in the exploitation plot. In the prediction phase, the trained RNN selects 100 NCHCF designs with the lowest predicted average CLs in the whole set. These 100 designs are then sorted according to the average simulated CLs over the selected spectral range. The final 100 best designs are listed in the video (supplementary material), in which the cross-section of a design is shown on the top and its CL spectrum is plotted on the bottom. The designs are labeled using two numbers. The first one indicates the index of the design in the final list whereas the second one indicates the index in the list given by the RNN. For example, RLD#1(#2) stands for the RL design (RLD) that is the best with respect to lowest average CL and the second best predicted by the RNN. The CL spectrum of each design is compared to that of NCHCF with three adjacent nested tubes [33] as a reference, which has the lowest average CL among all the proposed designs in literature. Further statistical analysis shows that the first 97 designs outperform this reference design in terms of average CL and its standard deviation over the selected wavelength range.

The top 100 designs can be sorted into two groups, which can be represented by two designs: RLD#2(#5) (Fig. 5 olive stars) and RLD#5(#1) (Fig. 5 orange pentagons). Fig. 5 compares the CL spectra of those two RL designs with selected 'conventional' NCHCF designs proposed in literature (black squares, red dots, blue triangles, green triangles, pink diamonds, yellow triangles, light blue triangles, and brown hexagons) [1], [2], [7], [27]–[31], [33], [34], [36], [37], [40]. The geometrical parameters of those 'conventional' designs have been optimized to achieve minimum average CLs in the wavelength range. All the designs in Fig. 5 have the same core radius of 4.9 μm. The two proposed novel designs show lower CLs at shorter wavelengths (240 nm–250 nm) and much lower CLs in the longer wavelength range (350 nm – 390 nm) when compared to the 'conventional' designs. Around

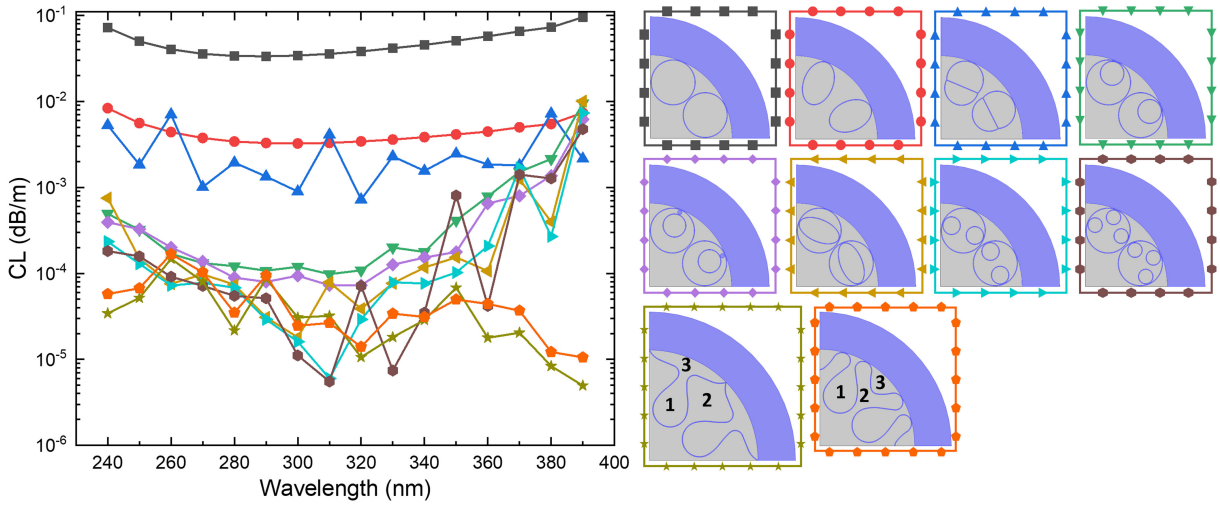

Fig. 5. CL spectra comparison (left) between two RL designs (last row on the right) and NCHCF designs proposed in literature (first two rows on the right). The line colors and symbols around the fiber quarter cross-sections correspond to the line colors and symbols in the CL spectra shown in the left part. The sizes of the cross-sections reflect their relative geometrical sizes. Note that the large capillary tubes in designs indicated by black squares, green triangles, pink diamonds, yellow triangles, light blue triangles, and brown hexagons are not touching. The numbers in the cross-sections of the RL designs indicate the negative curvature regions.

the center wavelength (315 nm), their CLs are at the same level as the 'conventional' designs with the lowest CLs. The average CL over the whole spectrum is 4.1×10^{-5} dB/m and 5.1×10^{-5} dB/m for RLD#2(#5) and RLD#5(#1), respectively. These compare favorably with the lowest average CL of 5.6×10^{-4} dB/m (capillaries with three adjacent nested tubes [33], brown hexagons) obtained for any of the previously proposed designs and are several orders of magnitude lower than the average CLs of other 'conventional' NCHCF designs.

IV. Discussion

The fabrication of these NCHCFs requires precise control of pressure during the stack-and-draw procedure. Nevertheless, the similarity among the best 100 designs suggests the robustness of these designs to fabrication variations. We attribute these RL designs' low CLs over a wide wavelength span to the following properties. First, by introducing non-circular cladding structures, the RL designs feature an extended cladding area and a more 'negative' capillary curvature. Both has been shown [26], [28], [29] to be effective in reducing CLs. Secondly, extra negative curvature regions, as indicated by the numbers in the quarter cross-section of the RL designs in Fig. 5, also help decreasing CLs. In other proposed designs [7], [27], [32]–[34], [36], [37], this is achieved by adding nested tubes. However, the touching points between the nested tubes and original tubes introduce extra optical resonators [22], which deteriorate the performance of the fiber. In the RL designs, on the other hand, extra negative curvature regions are achieved by modifying the capillary shape, making these designs free of extra optical resonators. Moreover, although not being optimized in terms of BL, RLD#2(#5) and RLD#5(#1) exhibit rather low BLs as well. Simulations show that the bending radius under which the BLs of these two RL designs increase by 3 dB is 2.5 cm.

Given the core radius and the operating wavelength range, the proposed method can be extended to search for low-average-CL NCHCFs with larger cross-section sizes and different numbers of unit structures in the cladding. Furthermore, by adjusting the reward signal to the BL under randomly picked bending radii and directions, HOMER, overlap of the optical mode with the capillary structure or a weighted average of these parameters, the method can be used to find structures with low BL, high HOMER, small overlap of the optical mode with the capillary or structures that achieve a trade-off among those parameters.

Despite of its success, several limitations of the current method should be noted as well. First, the number of unit structures in the cladding is fixed during the design process. To find the optimum number of unit structure for a given core radius, one needs to repeat the whole design process for different numbers of unit structures and, successively, compare the best designs. This can be improved in future work by including the number of unit structure as a tunable parameter and constructing an RNN for each case. Secondly, there are structures that are impossible or hard to be generated. The presented method of generating capillary structures by appending segments of rings limits the structures to Eulerian trails. Consequently, structures such as conjoined tubes [40] (Fig. 5, blue triangles) cannot be generated. Moreover, some designs are easier to be generated than others, which can make the whole set of designs loaded with similar designs. For example, NCHCFs with two nested adjacent tubes [34] (Fig. 5, cyan triangles) are rather unlikely to be generated. Thus, although helpful design suggestions have been already gained with our new approach, the design set in this paper is still far from enumerating all possible designs. Thirdly, the feasibility of fabrication has not been taken into consideration. However, parameters describing the fabrication difficulty, such as the change of the curvature radius of a capillary, can be included as a penalty in the reward signal.

In short, future efforts should invest in the development of a more sophisticated method of generating capillary structures to fully exploit the RL approach through even more diverse design studies. Future efforts can also include utilizing topology optimization [56] to tweak the capillary structure in NCHCFs. Topology optimization has been successfully applied to design the area around the core in HC-PBGFs in order to minimize energy loss [57]. This is an alternative approach to explore and exploit more diverse structures in the fiber cladding.

V. Conclusion

In this paper, we have proposed a novel method to find NCHCF designs with low CLs for a given core radius and operating wavelength range. We decompose the capillary cladding structures to segments of rings. By appending those segments, we construct a set containing 1,000,000 NCHCF designs. An RL method, in which an RNN and an FEM based modal solver interact with each other, has been used to search for the optimum design. The RNN selects a design while the FEM based modal solver provides the CL calculation of that design, which is in turn used to train the RNN. The resulting best NCHCF designs show low CLs over the entire operating wavelength span. The average CLs of the designs are more than one order of magnitude lower than the lowest average CL of designs in literature. The proposed method can also be used to study the optimum NCHCF designs in terms of BL, HOMER, overlap of the optical mode with the capillary structure or a combination of NCHCF properties.

References

[1] Y. Y. Wang, F. Couny, P. J. Roberts, and F. Benabid, "Low loss broadband transmission in optimized core-shape Kagome Hollow-Core PCF," in *Proc. Conf. Lasers Electro-Optics 2010, OSA Tech. Dig. (CD) (Opt. Soc. Amer.)*, 2010, Paper CPDB4.

[2] A. D. Pryamikov, A. S. Biriukov, A. F. Kosolapov, V. G. Plotnichenko, S. L. Semjonov, and E. M. Dianov, "Demonstration of a waveguide regime for a silica hollow–core microstructured optical fiber with a negative curvature of the core boundary in the spectral region >3.5 μm," *Opt. Express*, vol. 19, no. 2, pp. 1441–8, 2011.

[3] P. Roberts *et al.*, "Ultimate low loss of hollow-core photonic crystal fibres," *Opt. Express*, vol. 13, no. 1, pp. 236–244, 2005.

[4] M. A. Duguay, Y. Kokubun, T. L. Koch, and L. Pfeiffer, "Antiresonant reflecting optical waveguides in SiO_2 -Si multilayer structures," *Appl. Phys. Lett.*, vol. 49, no. 1, pp. 13–15, Jul. 1986.

[5] J.-L. Archambault, R. J. Black, S. Lacroix, and J. Bures, "Loss calculations for antiresonant waveguides," *J. Lightw. Technol.*, vol. 11, no. 3, pp. 416–423, Mar. 1993.

[6] N. M. Litchinitser, A. K. Abeeluck, C. Headley, and B. J. Eggleton, "Antiresonant reflecting photonic crystal optical waveguides," *Opt. Lett.*, vol. 27, no. 18, pp. 1592–1594, Sep. 2002.

[7] F. Poletti, "Nested antiresonant nodeless hollow core fiber," *Opt. Express*, vol. 22, no. 20, pp. 23807–23828, 2014.

[8] E. G. Rawson, "Theory of scattering by finite dielectric needles illuminated parallel to their Axes," *J. Opt. Soc. America*, vol. 62, no. 11, pp. 1284–1286, Nov. 1972.

[9] E. G. Rawson, "Analysis of scattering from fiber waveguides with irregular core surfaces," *Appl. Opt.*, vol. 13, no. 10, pp. 2370–2377, Oct. 1974.

[10] B. J. Mangan *et al.*, "Low loss (1.7 dB/km) hollow core photonic bandgap fiber," in *Proc. Opt. Fiber Commun. Conf. Techn. Dig. (CD) (Opt. Soc. Amer.)*, 2004, Paper PD24.

[11] M. H. Frosz, P. Roth, M. C. Günendi, and P. St. J. Russell, "Analytical formulation for the bend loss in single-ring hollow-core photonic crystal fibers," *Photon. Res.*, vol. 5, no. 2, pp. 88–91, Apr. 2017.

[12] B. Debord *et al.*, "Hypocycloid-shaped hollow-core photonic crystal fiber Part I: Arc curvature effect on confinement loss," *Opt. Express*, vol. 21, no. 23, pp. 28597–28608, Nov. 2013.

[13] A. W. Snyder and J. D. Love, *Optical Waveguide Theory*, Boston, MA, USA: Springer, 1984.

[14] L. Vincetti and V. Setti, "Waveguiding mechanism in tube lattice fibers," *Opt. Express*, vol. 18, no. 22, pp. 23133–23146, Oct. 2010.

[15] B. Debord *et al.*, "Ultralow transmission loss in inhibited-coupling guiding hollow fibers," *Optica*, vol. 4, no. 2, pp. 209–217, 2017.

[16] W. Ding and Y. Wang, "Analytic model for light guidance in single-wall hollow-core anti-resonant fibers," *Opt. Express*, vol. 22, no. 22, pp. 27242–27256, Nov. 2014.

[17] W. Ding and Y. Wang, "Semi-analytical model for hollow-core anti-resonant fibers," *Frontiers Phys.*, vol. 3, Mar. 2015.

[18] L. Vincetti and L. Rosa, "A simple analytical model for confinement loss estimation in hollow-core Tube Lattice Fibers," *Opt. Express*, vol. 27, no. 4, pp. 5230–5237, Feb. 2019.

[19] Y. Wang and W. Ding, "Confinement loss in hollow-core negative curvature fiber: A multi-layered model," *Opt. Express*, vol. 25, no. 26, pp. 33122–33133, Dec. 2017.

[20] A. D. Pryamikov, G. K. Alagashev, A. F. Kosolapov, and A. S. Biriukov, "Impact of core-cladding boundary shape on the waveguide properties of hollow core microstructured fibers," *Laser Phys.*, vol. 26, no. 12, Dec. 2016, Art. no. 125104.

[21] A. D. Pryamikov and G. Alagashev, "Features of light leakage from the negative curvature hollow core fibers," *Opt. Eng.*, vol. 57, no. 06, pp. 1–7, Jun. 2018.

[22] A. N. Kolyadin, A. F. Kosolapov, A. D. Pryamikov, A. S. Biriukov, V. G. Plotnichenko, and E. M. Dianov, "Light transmission in negative curvature hollow core fiber in extremely high material loss region," *Opt. Express*, vol. 21, no. 8, pp. 9514–9519, 2013.

[23] F. Yu and J. C. Knight, "Spectral attenuation limits of silica negative curvature hollow core fiber," *Opt. Express*, vol. 21, no. 18, pp. 21466–21471, Sep. 2013.

[24] W. Belardi and J. C. Knight, "Effect of core boundary curvature on the confinement losses of hollow antiresonant fibers," *Opt. Express*, vol. 21, no. 19, pp. 21912–7, 2013.

[25] L. D. van Putten *et al.*, "Exploring the effect of the core boundary curvature in hollow antiresonant fibers," *IEEE Photon. Technol. Lett.*, vol. 29, no. 2, pp. 263–266, Jan. 2017.

[26] L. Vincetti, "Empirical formulas for calculating loss in hollow core tube lattice fibers," *Opt. Express*, vol. 24, no. 10, pp. 10313–10325, May 2016.

[27] W. Belardi and J. C. Knight, "Hollow antiresonant fibers with reduced attenuation," *Opt. Lett.*, vol. 39, no. 7, pp. 1853–1856, Apr. 2014.

[28] Md. S. Habib, O. Bang, and M. Bache, "Low-loss single-mode hollow-core fiber with anisotropic anti-resonant elements," *Opt. Express*, vol. 24, no. 8, pp. 8429–8436, Apr. 2016.

[29] S. Chaudhuri, L. D. Van Putten, F. Poletti, and P. J. A. Sazio, "Low loss transmission in negative curvature optical fibers with elliptical capillary tubes," *J. Lightw. Technol.*, vol. 34, no. 18, pp. 4228–4231, Sep. 2016.

[30] F.-C. Meng, B.-W. Liu, Y.-F. Li, C.-Y. Wang, and M.-L. Hu, "Low loss hollow-core antiresonant fiber with nested elliptical cladding elements," *IEEE Photon. J.*, vol. 9, no. 1, Feb. 2017, Art. no. 7100211.

[31] Y. Han, F. Meng, S. Qiu, T. Dong, W. Zhu, and Y. Qing, "Low loss negative curvature fiber with circular internally tangent nested tube in elliptical tubes," in *Proc. Tenth Int. Conf. Inf. Opt. Photon.*, Beijing, China, 2018, pp. 332–336.

[32] M. S. Habib, O. Bang, and M. Bache, "Low-loss hollow-core anti-resonant fibers with semi-circular nested tubes," *IEEE J. Sel. Top. Quantum Electron.*, vol. 22, no. 2, pp. 156–161, Mar./Apr. 2016.

[33] Md. S. Habib, O. Bang, and M. Bache, "Low-loss hollow-core silica fibers with adjacent nested anti-resonant tubes," *Opt. Express*, vol. 23, no. 13, pp. 17394–17406, Jun. 2015.

[34] G. T. Jasion, D. J. Richardson, and F. Poletti, "Novel antiresonant hollow core fiber design with ultralow leakage loss using transverse power flow analysis," in *Proc. Opt. Fiber Commun. Conf. (OFC) 2019*, San Diego, California, 2019, Paper Th3E.2.

[35] T.-Y. Yu, X. Liu, and Z.-W. Fan, "Hollow core antiresonant fiber with radially asymmetric nodeless claddings," *IEEE Photon. J.*, vol. 10, no. 1, pp. 1–8, Feb. 2018.

[36] M. I. Hasan, N. Akhmediev, and W. Chang, "Positive and negative curvatures nested in an antiresonant hollow-core fiber," *Opt. Lett.*, vol. 42, no. 4, pp. 703–706, 2017.

[37] Md. S. Habib, J. E. Antonio-Lopez, C. Markos, A. Schülzgen, and R. Amezcua-Correa, "Single-mode, low loss hollow-core anti-resonant fiber designs," *Opt. Express*, vol. 27, no. 4, pp. 3824–3836, Feb. 2019.

[38] Y. Chen, M. F. Saleh, N. Y. Joly and F. Biancalana, "Low-loss single-mode negatively curved square-core hollow fibers," *Opt. Lett.*, vol. 42, no. 7, pp. 1285–1288, 2017.

[39] M. Banu *et al.*, "Lotus-shaped negative curvature hollow core fiber with 10.5 dB / km at 1550 nm wavelength," *J. Lightw. Technol.*, vol. 36, no. 5, pp. 1213–1219, Mar. 2018.
[40] S. Gao and Y. Wang, "Hollow-core conjoined-tube negative-curvature fibre with ultralow loss," *Nature Commun.*, vol. 9, no. 1, pp. 1–6, 2018.
[41] T. D. Bradley, J. R. Hayes, Y. Chen, G. T. Jasion, S. R. Sandoghchi, and R. Slavik, "Record low-loss 1.3dB / km data transmitting antiresonant hollow core fibre," in *Proc. Eur. Conf. Opt. Commun.*, Rome, 2018, no. 1, pp. 1–3.
[42] R. S. Sutton and A. G. Barto, *Reinforcement Learning: An Introduction*, Cambridge, Mass: MIT, 1998.
[43] S. B. Kotsiantis, "Supervised machine learning: A review of classification techniques," *Informatica*, vol. 31, pp. 249–268, 2007.
[44] F. Musumeci, C. Rottondi, A. Nag, D. Zibar, M. Ruffini, and S. Member, "An overview on application of machine learning techniques in optical networks," *IEEE Commun. Surveys Tut.*, vol. 21, no. 2, pp. 1383–1408, Apr./Jun. 2019.
[45] J. Bueno *et al.*, "Reinforcement learning in a large-scale photonic recurrent neural network," *Optica*, vol. 5, no. 6, pp. 756–760, 2018.
[46] M. Naruse, Y. Terashima, A. Uchida, and S.-J. Kim, "Ultrafast photonic reinforcement learning based on laser chaos," *Sci. Rep.*, vol. 7, no. 1, Dec. 2017, Art. no. 8772.
[47] M. Alonzo, D. Moscatelli, L. Bastiani, A. Belardini, C. Soci, and E. Fazio, "All-Optical Reinforcement Learning In Solitonic X-Junctions," *Sci. Rep.*, vol. 8, no. 1, Dec. 2018, Art. no. 5716.
[48] H. Robbins, "Some aspects of the sequential design of experiments," *Bull. Amer. Math. Soc.*, vol. 58, no. 5, pp. 527–535, Sep. 1952.
[49] T. L. Lai and H. Robbins, "Asymptotically efficient adaptive allocation rules," *Adv. Appl. Math.*, vol. 6, no. 1, pp. 4–22, Mar. 1985.
[50] Z. C. Lipton, J. Berkowitz, and C. Elkan, "A critical review of recurrent neural networks for sequence learning," *arXiv:1506.00019*, May 2015.
[51] X. Glorot, A. Bordes, and Y. Bengio, "Deep sparse rectifier neural networks," in *Proc. Fourteenth Int. Conf. Artif. Intell. Statist.*, pp. 315–323, 2011.
[52] S. Hochreiter and J. Schmidhuber, "Long short-term memory," *Neural Comput.*, vol. 9, no. 8, pp. 1735–1780, Nov. 1997.
[53] D. E. Rumelhart, G. E. Hinton, and R. J. Williams, "Learning representations by back-propagating errors," *Nature*, vol. 323, no. 6088, pp. 533–536, Oct. 1986.
[54] X. Glorot and Y. Bengio, "Understanding the difficulty of training deep feedforward neural networks," *J. Mach. Learn. Res.*, vol. 9, pp. 249–256, 2010.
[55] D. P. Kingma and J. Ba, "Adam: A method for stochastic optimization," *arXiv:1412.6980*, Dec. 2014.
[56] M. P. Bendsøe and N. Kikuchi, "Generating optimal topologies in structural design using a homogenization method," *Comput. Methods Appl. Mechanics Eng.*, vol. 71, no. 2, pp. 197–224, Nov. 1988.
[57] M. B. Dühring, O. Sigmund, and T. Feurer, "Design of photonic bandgap fibers by topology optimization," *J. Opt. Soc. Am. B*, vol. 27, no. 1, pp. 51–58, Jan. 2010.

Xiaowen Hu received the B.S. degree in optical science and technology from Fudan University, Shanghai, China, in 2015. He is currently working toward the Ph.D. degree in optics and photonics with CREOL, The College of Optics and Photonics, University of Central Florida, Orlando, FL, USA. His research interests include microstructured fiber optics, machine learning applications in optics and optical fiber imaging.

Axel Schülzgen (Fellow, OSA) received the Ph.D. degree in physics from the Humboldt University of Berlin, Berlin, Germany. Since 2009, he has been a Professor of Optics and Photonics with CREOL, The College of Optics and Photonics, University of Central Florida, Orlando, FL, USA. He also holds an Adjunct Research Professor position with the College of Optical Sciences, University of Arizona, AZ, USA. He has authored more than 130 scientific publications in peer reviewed journals, more than 60 invited talks at international conferences, and six patents. His current research interests include optical fiber devices, components, materials, and structures with applications in fiber laser systems, fiber optic sensing and imaging, and optical communications. He is a Fellow of the Optical Society of America.